Supplementary Information for

Conformational Entropy of a Single Peptide Controlled Under Force Governs Protease Recognition and Catalysis

Marcelo E. Guerin [1,2,3], Guillaume Stirnemann [4], David Giganti [5]

[1] Structural Biology Unit, CIC bioGUNE, Bizkaia Technology Park, 48160 Derio, Spain.

[2] Unidad de Biofísica, Centro Mixto Consejo Superior de Investigaciones Científicas, Universidad del País Vasco, Leioa, Bizkaia 48940, Spain; Departamento de Bioquímica, Universidad del País Vasco, Leioa, Bizkaia 48940, Spain; Universidad del País Vasco/Euskal Herriko Unibertsitatea (CSIC, UPV/EHU), Barrio Sarriena s/n, Leioa, Bizkaia 48940, Spain.

[3] IKERBASQUE, Basque Foundation for Science, 48011 Bilbao, Spain.

[4] CNRS, Laboratoire de Biochimie Théorique, Institut de Biologie Physico-Chimique, Univ. Paris Denis Diderot, Sorbonne Paris Cité, PSL Research University, 13 rue Pierre et Marie Curie, 75005 Paris, France.

[5] Randall Division of Cell and Molecular Biophysics, King's College London, London, United Kingdom.

This file includes:

1. Supplementary Materials and Methods

1.1. Cloning, protein expression and purification
1.2. Data collection and analysis
1.3. Steered Molecular Dynamics simulations

2. Supplementary Figures

Figure S1: Limited proteolysis of substrates with different solvent accessibility.
Figure S2: Mechanical unfolding of $(\mathrm{I27\Delta TevSite})_8$.
Figure S3: Relaxation of the chain during the 170pN-60pN transition.
Figure S4: Control conditions, experimental traces.
Figure S5: Probability of rupture due to detachment or cleavage.
Figure S6: Rapid activation of the reaction and release of the product.
Figure S7: Ramachandran maps calculated from Steered Molecular Dynamics simulations.
Figure S8: Local curvature of the backbone decreases with force.
Figure S9: Comparison of the SMD and TEMPE approaches.
Figure S10: Role of conformational entropy upon the binding
Figure S11: Estimation of the kinetic parameters from simulated dwell-time distributions

3. Supplementary Tables

Table S1: Reactions rates retrieved from the dependence on the enzyme concentration and on the force applied to the substrate
Table S2: Dihedrals of the substrate backbone in the bound conformation
Table S3: Conformational entropy for the modeling of the force dependent reaction rates.

4. Supplementary Movie

Movie S1: TEMPE (Torsional Free Energy Model of Protein Elasticity) maps from 0 to 500pN

5. Supplementary References

1. Supplementary Materials and Methods

1.1. Cloning, Protein Expression and Purification

In the (I27ΔTevSite)$_8$ construct, the two C-terminal Cys are required for the covalent attachment to a gold surface (see the section Atomic Force Spectroscopy experiments) while the N-terminal His-Tag allows the first purification step based on step immobilized metal-ion affinity. The cDNA coding for the final octamer was cloned in the plasmid pQE80L (QIAGEN) to produce the recombinant protein with the following sequence:

MRGSHHHHHHGSLIEVEKPLYGVEVFVGETAHFEIELENLYFQ↕GQWKLKGQPLAASPDC
EIIEDGKKHILILHNCQLGMTGEVSFQAANTKSAANLKVKELRSLIEVEKPLYGVEVFVGET
AHFEIELENLYFQ↕GQWKLKGQPLAASPDCEIIEDGKKHILILHNCQLGMTGEVSFQAANTK
SAANLKVKELRSLIEVEKPLYGVEVFVGETAHFEIELENLYFQ↕GQWKLKGQPLAASPDCEI
IEDGKKHILILHNCQLGMTGEVSFQAANTKSAANLKVKELRSLIEVEKPLYGVEVFVGETA
HFEIELENLYFQ↕GQWKLKGQPLAASPDCEIIEDGKKHILILHNCQLGMTGEVSFQAANTKS
AANLKVKELRSLIEVEKPLYGVEVFVGETAHFEIELENLYFQ↕GQWKLKGQPLAASPDCEII
EDGKKHILILHNCQLGMTGEVSFQAANTKSAANLKVKELRSLIEVEKPLYGVEVFVGETAH
FEIELENLYFQ↕GQWKLKGQPLAASPDCEIIEDGKKHILILHNCQLGMTGEVSFQAANTKSA
ANLKVKELRSLIEVEKPLYGVEVFVGETAHFEIELENLYFQ↕GQWKLKGQPLAASPDCEIIE
DGKKHILILHNCQLGMTGEVSFQAANTKSAANLKVKELRSLIEVEKPLYGVEVFVGETAHF
EIELENLYFQ↕GQWKLKGQPLAASPDCEIIEDGKKHILILHNCQLGMTGEVSFQAANTKSAA
NLKVKELRSCC

where the TEV cleavage site in underlined and the scissile peptide bond marked by ↕. We transformed BLR (DE3) *E. coli* expression strains and incubated the cell cultures in LB medium (supplemented with 100 μg.ml^{-1} ampicillin) at 37°C until the OD$_{600}$ reaches ~0.6. The expression of (I27ΔTevSite)$_8$ was induced by adding 1mM isopropyl β-D-1-thiogalactopyranoside. After ~16 hs at 20°C, cells were collected at 4,000*g* for 10 min and resuspended in PBS buffer containing protease inhibitors (Complete EDTA-free, Roche). Cells were disrupted by adding Lysozyme (1mg. ml^{-1}), 1% Triton-X100, 10mM MgCl$_2$, DNAse I (5 μg.ml^{-1}), and RNAse (5 μg.ml^{-1}), and applying two cycles in a French Press. We used a standard protocol for the purification (1). The clarified lysate was applied to a Talon resin (Clontech) for a metal affinity chromatography followed by a gel filtration on a Superdex 200 10/300 GL column (GE Biosciences) equilibrated with the final experimental buffer EB (150 mM Hepes pH 7.2, 150mM NaCl, 10mM EDTA). The resulting sample revealed a unique protein band on a 12% SDS-PAGE gel. The protein was stable for 1 week at 4°C. Identical procedure was used for the I27 wild type octamer. The 27 kDa engineered Tev protease(2) was produced and purified with a standard protocol, as previously described (2). We exchanged the buffer by dialysis to the final buffer EB + 0.1 mM tris(2-carboxyethyl)phosphine (TCEP), and we concentrated the purified sample with centrifugal filters (Amicon) to ~50μM. Final samples were aliquoted with argon to prevent oxidation and stored at -80°C. Protein concentration was determined with a Bradford assay and verified after dilution from frozen concentrated samples.

1.2 Data collection and analysis

For each experiment, several force protocols conditions were tested to avoid possible artefacts and verify the consistency of measurements obtained from different days. Experiments were running automatically for a few hours (~1 to 8 hours, depending on the tested condition) at room temperature and only traces lasting through the end of the first pulse were visually analyzed. Productive traces were selected based on the presence during the first force pulse (170pN) of steps that could be attributed to the unfolding of I27ΔTevSite domains and the absence of alternative marked increment of the protein extension along the trace. Our typical force protocol is 30-second long and terminates with a high force pulse (2000pN) that triggers the instantaneous detachment of the tethered substrate.

All analyses have been carried out with Igor Pro 6.2 (Wavemetrics) and Python2.7. For each condition (force and concentration of protease), dwell times were normalized by the number of unfolding events (except figure 2B). We generated sub-datasets of normalized dwell times from 1,000 bootstrap iterations, then computed the cumulative dwell-time histograms (binsize=0.01s), and finally measured from each subset histogram the rupture rate $k_{rupture}$ or k_r with an exponential regression that fits the equation eq.1

$$p_{rupture}(t) = 1 - 1\,.\,e^{-k_r.t} \qquad \text{eq.1}$$

$p_{rupture}$ being the histogram density probability. Finally, we generated a histogram of the $k_{rupture}$, obtained from the bootstrap, that fits a Gaussian distribution used to obtain the final rate and associated standard error s.e. (mean and σ parameters extracted from the modeled Gaussian). These final values as reported in the text as $k_{rupture}$ ± s.e. are also used to produce, in the figures, the curves modelling the single exponential decay of the dwell-time probability.

In the Figure 4A, the combined effect of normalization and the enlarged data size reveals a distribution of dwell times τ_r that deviates from a single exponential decay, suggesting the ability to detect a reaction intermediate. We propose a simple kinetic model $E + S \rightarrow E.S \rightarrow E + P$ where k_{on} denotes the second order rate to form the complex E.S and k_{cat} is the catalytic rate to form the product P. In the particular case of our study, we neglect the dissociation rate of the complex E.S ($k_{off} = 0$) because the release of the substrate seems to occur at a rate considerably slower than the catalysis (i.e. k_{cat}~$0.8s^{-1}$). Indeed, Xray structures of the holo enzyme in complex with its substrate (pdb: *1lvb*) or the product (pdb: *1lvm*) suggest a high affinity evidenced by a dense network of hydrogen bonds and large hydrophobic contacts stabilizing the complex interface (3, 4). Furthermore, a previous study confirmed with Isothermal Titration Calorimetry a high affinity, divulging a Kd in a low μM range (4). Finally, we tested a kinetic model (variant of eq. 3) that includes the dissociation k_{off} corresponding to the transition $E + S \rightarrow E.S$. We obtained similar fits and values of k_{on} and k_{cat} while $k_{off} << k_{cat}$.

In our experiments, a single substrate is followed as the enzyme concentration in the system can be considered as constant [E] ~ $[E]_0$. In solving the kinetics equations, the situation is therefore identical to the case of a single enzyme in the presence of a fixed concentration of substrate (5). The dwell-time distribution f(t) corresponds to:

$$f(t) = \left(\left(\frac{kon.kcat.[E]_0}{kcat - kon.[E]_0}\right)\left(e^{-kon.[E]_0.t} - e^{-kcat.t}\right)\right) \qquad \text{eq.2}$$

We therefore obtained the parameters k_{on} and k_{cat} from the distribution of dwell times τ_r. In order the test the robustness of the fit to the histogram, we were able to characterized the presence of a kinetic intermediate and recover similar values of k_{cat} (0.73 to 0.79 s^{-1}) for different number of bins, varying from 20 to 1000. In addition, we confirmed with simulated data that the dataset in figure 4A contains enough measurements for a reliable fit and estimation of the parameters (figure S11).

Alternatively, we can retrieve the reaction constants k_{on} and k_{cat} by varying the concentration of enzyme present in solution. The figure 4D shows that at a given force, the reaction rate $k_{rupture}$ increases with the concentration of enzyme [Enzyme]=$[E]_0$. Reaction rates constants show a clear hyperbolic saturation that confirms that the overall rate $k_{rupture}$ or k_r is govern by one first order rate (k_{cat}) while the second order association rate (k_{on}) is proportional to enzyme concentration. At high concentration, the *kcat* becomes the exclusive rate limiting-step. The average reaction rate $k_{rupture}$ can be deduced from the first moment of the waiting time distribution of eq 1 (Single-Molecule Michaelis Menten equation neglecting k_{off}, eq. 14 derived by *Kou et al.*(6)), such that

$$k_r = \frac{kcat.[E]_0}{[E]_0 + \frac{kcat}{kon}} \qquad \text{eq.3}$$

This model is equivalent to the equation $k_r = \left(\frac{1}{kon.[E]_0} + \frac{1}{kcat}\right)^{-1}$ used by Van Den Broek *et al.* for a linear reaction chain (7). The resulting fits revealed that k_{on} is largely affected by the force while k_{cat} changes only moderately. In the figure 4D, the determination of the plateau is necessary to pin down with precision the value of k_{cat}. Therefore, the characterization of the catalytic rate at 80pN or 100pN requires conditions of high enzyme concentration that are incompatible with the feasibility of our experiments (e.g. limitations due to the enzyme solubility or fast degradation of the substrate due to transient thermal unfolding). We cannot conclude on the relevance of this modest change of k_{cat}. Nevertheless, comparing the rates determined at 60pN and 100pN, we observed that k_{on} drops by one order of magnitude whereas k_{cat} decreases only by a factor 0.71 (see Table S1). The rates presented in figure 4D and associated values are obtained for a fixed k_{cat} = 0.80 s^{-1}. To test the possibility of an effect of the dissociation E.S on the measured kinetics, we used the original Single-Molecule Michaelis Menten equation (6) fitted to the experimental data. We could obtain a good fit with similar values k_{on} and k_{cat} while the constant k_{off} indicated a significantly slower dissociation ($k_{off} << k_{cat}$) .

1.3 Steered Molecular Dynamics Simulations

We constructed with Pymol (Version 1.8 Schrödinger, LLC) an extended chain composed of 100 alanine amino acids (centi-alanine). The chain was solvated in an orthorhombic water box of 2.5*2.5*50 nm, so that the chain and the box long axes were aligned in the z direction. We employed CHARMM36 parameters for protein atoms, while water molecules were described using the TIP3P-CHARMM force-field. Steered Molecular Dynamics (SMD) simulations were performed with the NAMD2.10 software (8). Long-range electrostatics were computed with Particle-Mesh Ewald. Temperature and pressure were maintained constant along the simulation. The carbon alpha of the first residue was maintained fixed, while the carbon alpha of the last residue was subject to a constant force along the z direction. The system was first minimized for 2,000 steps using a steepest-descent algorithm, and later equilibrated for 10 ns at a force of 200 pN. The force was then kept at this value, or changed toward 50, 100, 150, or 500 pN. Each system was then further equilibrated for 10 ns at this new force, and simulations were finally propagated for 30 ns. Equilibration as each force was ensured by following the relaxation of the end-to-end distance toward a constant value after a few nanoseconds at most. From the production runs, we collected 1,000 snapshots every 3 ps. Trajectories were analyzed with customized Python programs implemented with the Bio.PDB library.

2. Supplementary Figures

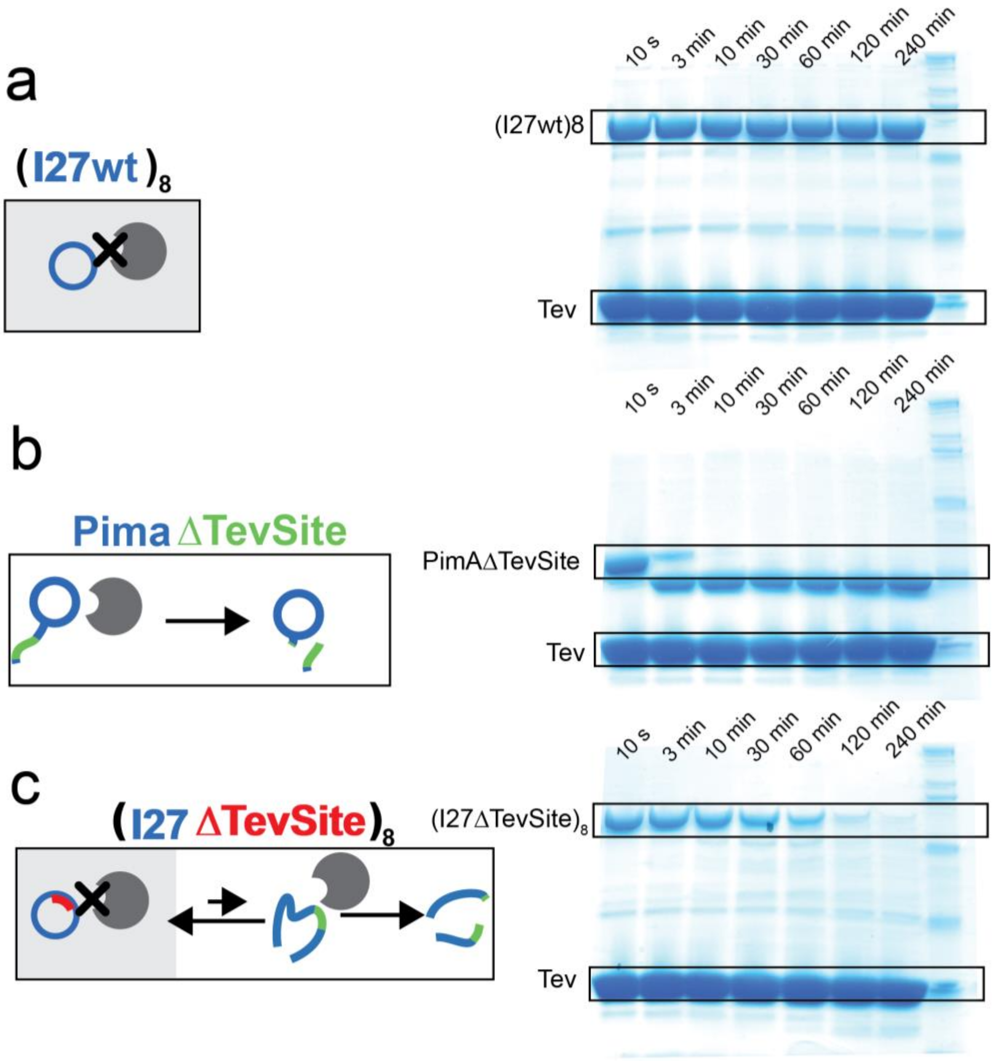

Fig. S1

Limited proteolysis of substrates with different solvent accessibility. A prerequisite for an effective digestion is the solvent accessibility of the substrate that must accommodates in the protease binding site before the catalysis. We investigated with a bulk assay the accessibility of the TevSite monitoring the digestion efficiency. With electrophoretic separation based on sodium dodecyl sulfate polyacrylamide gels (SDS-PAGE), we followed over time (from 10 seconds to 240 minutes) the degradation of the three different substrate ($(I27wt)_8$, PimaΔTevSite and $(I27\Delta Tevsite)_8$) into lower-mass products at high concentration ([Tev]= 250μM). I27wt is the native I27 domain. The excess of enzyme (factor of 5) mimics the environment of the single-molecule experiments (room temperature) where all enzymes are in a free state, contrasting with typical conditions of substrate excess used for Michaelis-Menten kinetics. ***a.*** In the first SDS-gel, we verified that $(I27wt)_8$ (upper band, 98kDa) is not digested in presence of Tev (lower band, 27kDa), corroborating with the absence in I27wt of the consensus sequence recognized by the Tev enzyme (E-Xaa-Xaa-Xaa-Xaa-Q↕G/S where Xaa can be any amino acid) (3, 9). ***b.*** In the PimaΔTevSite construct, the TevSite separates a N-terminal Histag from the N-terminal domain of PimA. The addition of the spacer in this construct (Histag-ENLYFQ↕G-spacer-PimA) was crucial for an optimal accessibility and a rapid digestion (10) leading to a complete digestion in less than 10 minutes ***c.*** In contrast, the same experiment with (I27ΔTevSite)$_8$ shows a slower digestion (~30 times) despite the presence of the identical ENLYFQ↕G sequence. The slower reaction is possibly due to the low accessibility of the TevSite in the folded I27ΔTevSite (Fig. 1C). Probably, the local fluctuations in I27ΔTevSite transiently exposed the vulnerable cleavage site. This mechanism is fundamental in limited proteolysis experiments to study the structural dynamics of proteins (11). Here, we cannot distinguish two different conceptions of a “buried site” that can be viewed either as unexposed to the solvent or trapped in an inactive conformation. The residue G69 in I27wt (pdb: *1TIT*) (phi = -162°, psi = -140°) differs from the conformation observed in the Tev complex is (phi = -85°, psi = 165°). The slow transition between the two states can explain the inefficient proteolysis. Similarly, our single-molecule approach relies on the changing accessibility of the cleavage site while the substrate unfolds and stretches under a pulling force

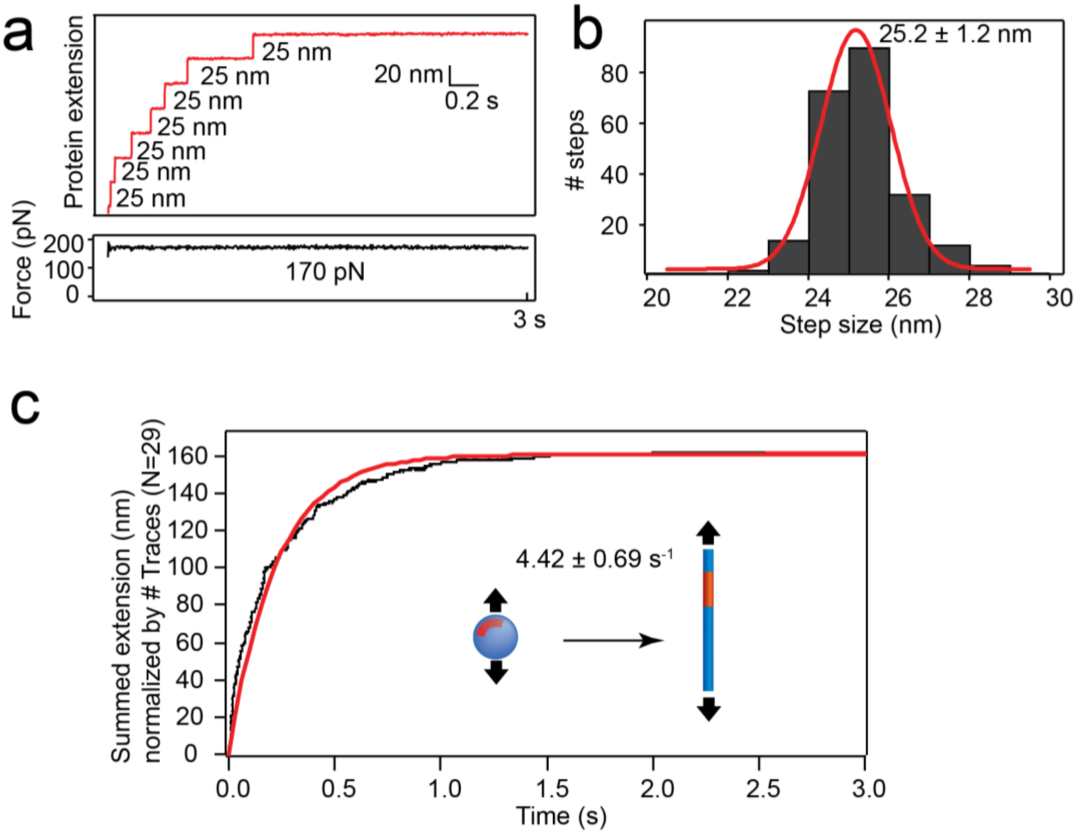

Fig. S2

Mechanical unfolding of (I27ΔTevSite)$_8$. ***a.*** This trace recorded at a constant force (170pN) shows the typical stepwise unfolding of (I27ΔTevSite)$_8$ marked by the repeated ~25 nm increment due to the rupture and extension of individual I27ΔTevSite domains. ***b.*** The histogram of the step size indicates an average value that matches the theoretical extensions of I27wt and I27ΔTevSite (both proteins share the same number of amino acids)(12). A Gaussian fit (red line) indicates an average step size of 25.2 ± 1.2 nm. ***c.*** The time course of unfolding events is evaluated by summing 29 traces (black line) and fitting a single exponential (red line) that provides the unfolding rate $k_{unfolding,170pN} = 4.42 \pm 0.69\ s^{-1}$. This value implies that all domains are expected to be extended at the end of the first pulse (3s at 170pN). Standard error of the rate constant is obtained from bootstrapping.

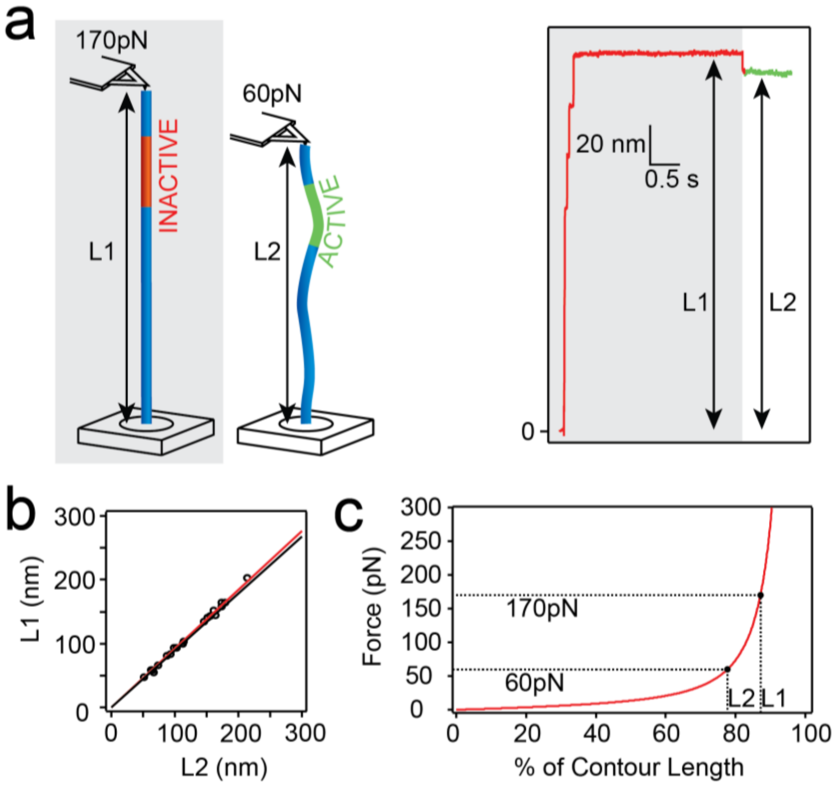

Fig. S3

Relaxation of the chain during the 170pN-60pN transition. ***a.*** At 170pN, the protein stretches up to a L1 length while the chain equilibrates to a shorter length L2 at 60pN (see schematics). The recording illustrates the resulting change of the protein extensions. The moderate difference in length enhances the conformational activation of the reaction (red to green color code) ***b.*** We report in this graph the L1 and L2 extensions from 20 representative traces (black circle, 52<L1<214nm and 47<L2<203nm). L1 and L2 depend on the attachment point, which varies from one recording to another. These two lengths are linearly correlated (L2/L1 = 0.92, red line). The theoretical ratio L2/L1 obtained from the Worm-like Chain model (persistence length p=0.36nm) displays a similar value (L2/L1= 0.89, black line) ***c.*** Force-extension curve calculated for a Worm-Like Chain (p = 0.36nm, Contour Length Lc = 100nm).

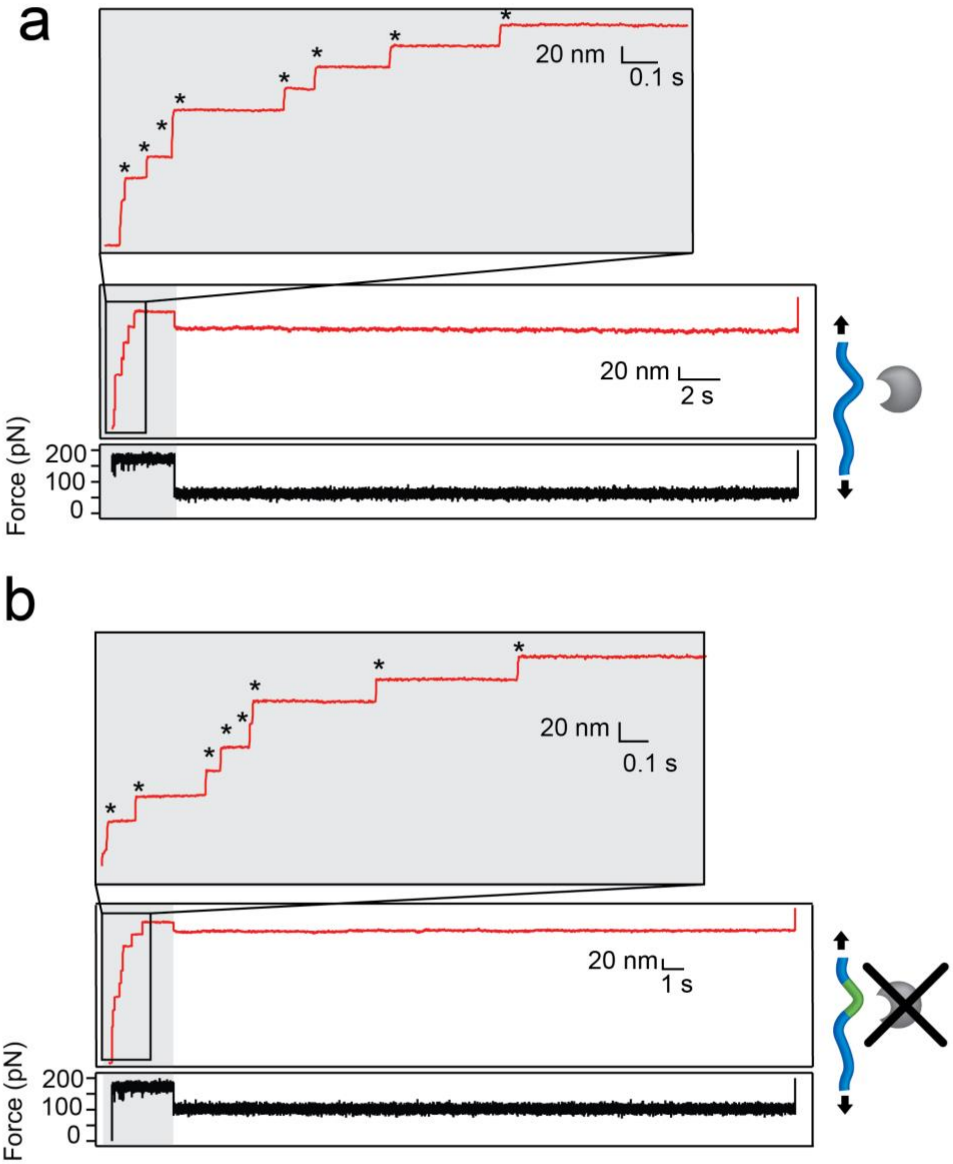

Fig. S4

Control conditions, experimental traces. ***a.*** Stretching of $(I27wt)_8$ in the presence of protease (9μM). TevSite mutation is absent in the native I27wt. During the unfolding pulse (grey background, 3s at 170pN), I27wt domains unfold (individual events are marked by an asterisk). During the probe pulse (30s at 60pN), the tension on the extended polyI27 substrate remains intact until the deliberate detachment triggered at the end of the pulse (force pulse at 2000pN). 37% of traces show a detachment before 30s. In contrast, 100% of traces show a rupture in the first 5s when the cleavage of $(I27\Delta TevSite)_8$ can occur in presence of enzyme. This confirms that I27wt prevents the proteolytic reaction. ***b.*** In addition, we undertook a second control experiment stretching $(I27\Delta TevSite)_8$ in absence of enzyme. We obtained similar traces. No detachment is observed in 35% of traces. Thoughtful washing of the fluid cell was required before setting this experiment to avoid traces of enzyme.

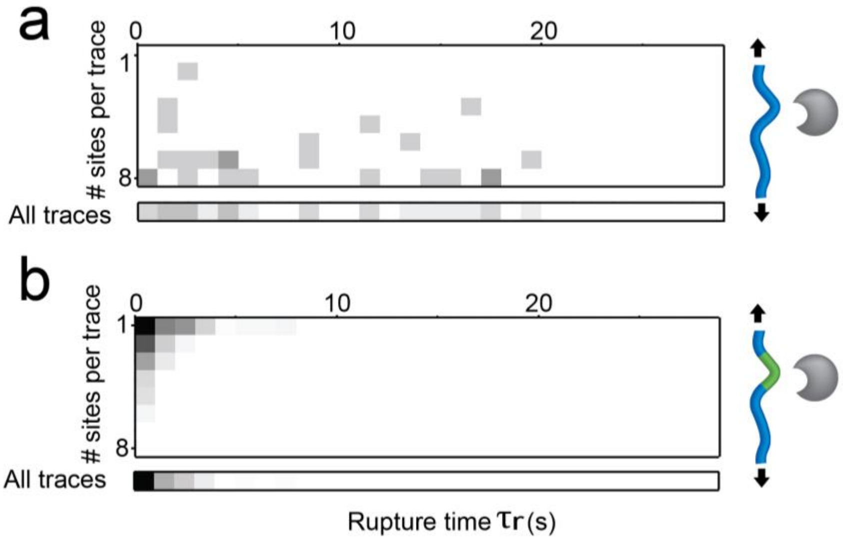

Fig. S5

Probability of rupture due to detachment or cleavage. We computed density maps to display the occurrence of rupture during the probe pulse. For each experimental condition, the upper map shows the waiting-time before detachment observed along the 30-second-long probe. The lower density bar is obtained for all summed traces, independently to the number of unveiled sites. **a.** In absence of cleavage site in I27wt (no TevSite mutation), occasional detachments happen independently to the number of unfolding events observed in the first pulse. **b.** When the cleavage site is accessible in $(I27\Delta TevSite)_8$, the rupture is drastically accelerated and displays a strong correlation with the number of accessible sites in the unfolded substrate. In conclusion, the two competitive mechanisms of cleavage and detachment show significantly different kinetics. This difference becomes more evident when the apparent rupture rate is increased when several sites are accessible and at high concentration of enzyme. Although the scenario of the rupture (i.e. cleavage or detachment) remains elusive for individual traces, the impact of detachment is modest in the overall rate measurement due to large statistics based on the rapid dwell-times obtained in our experimental conditions.

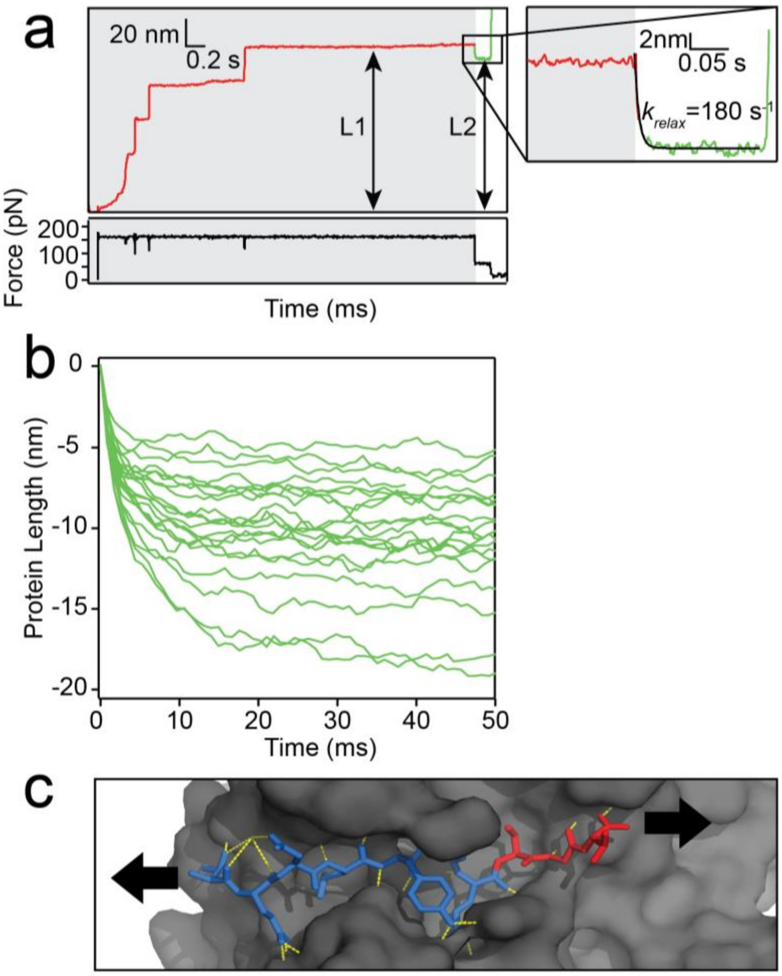

Fig. S6

Rapid activation of the reaction and release of the product. *a.* We observed a rapid equilibration of the chain length when the force drops from 170pN to 60pN. The shortening of the protein length fits an exponential decay (black fit in the left inset, rate of relaxation=180 s^{-1}). ***b.*** From 20 representative traces with different extensions (52<L1<214nm or 47<L2<203nm), we extracted the fraction of trace corresponding to the first 50ms of the probe pulse. The average relaxation is 240s^{-1} and remains fast for different values of L1. The relaxation is largely faster (>100-fold) than the enzymatic reaction so that we can ignore its fast kinetics for the calculation of the rupture dwell time. In addition, we tried to repeat the experiments at low probing force (<40pN) but often, we observed a complete collapse of the chain, probably due to the contacts between residues (e.g. hydrophobic interactions) making our approach based on the dynamics of extended chains irrelevant. **c.** The cleavage occurs in the C-terminal region of the substrate motif. The structure of the full substrate in the inactive enzyme (pdb: *1LVB*) shows that the P6-P1 fragment (blue) is stabilized by several polar contacts (yellow dotted line) and large hydrophobic patches whereas the P1'-P2' (red) associates through only three polar contacts. We expect that the cleavage triggers the quick detachment of P1'-P2' accelerated by the applied end-to-end force (black arrows). Moreover, the structure of the active enzyme obtained in presence of the substrate (pdb: *1LVM*) supports this hypothesis because only the P6-P1 is visible in the structure corroborating a low affinity of P1’-P2’ at 0 force. Finally, we could not detect kinetic intermediates related to the rapid relaxation of the chain or release of the product.

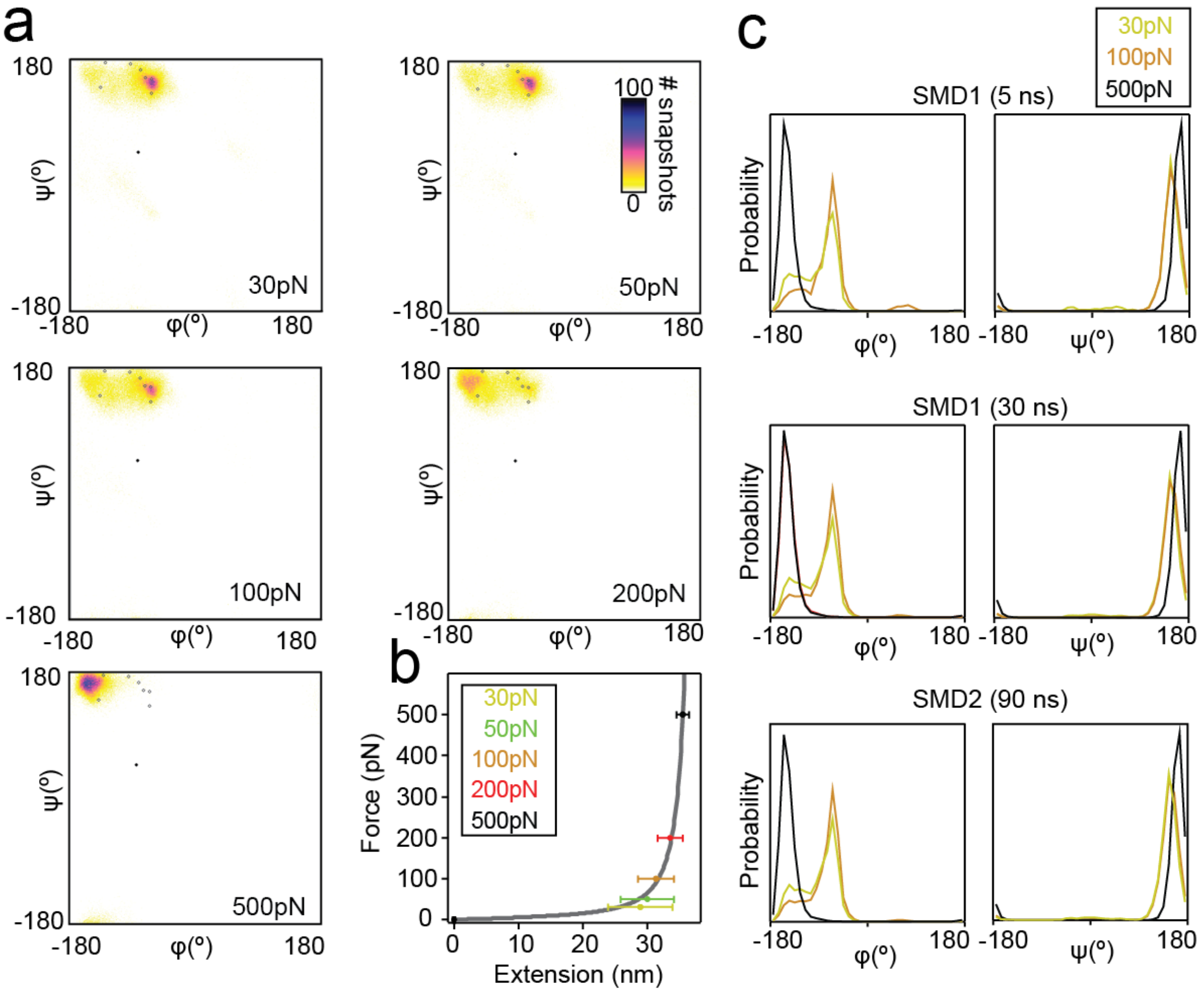

Fig. S7

Ramachandran maps calculated from Steered Molecular Dynamics simulations. a. For each SMD trajectory obtained at 30pN, 50pN, 100pN, 200pN and 500pN, we measured all (φ,ψ) couples along the chain (except the first and last residues). The resulting Ramachandran maps illustrate the density of (φ,ψ) angles measured in the simulation snapshots. Bound conformation of the residues P6-P2’ are marked with black circle markers. The curved conformation of the residue P1 (filled circle, φ=-90°, ψ=46°) corresponds to a high energy state that cannot be accurately sampled in our SMD simulations. **b.** The end-to-end distance measured along the trajectories fits well the Worm Like Chain Model (persistence length *p* = 0.36nm) (13). **c.** Ensemble of accessible backbone conformations along the trajectory. Distributions of φ and ψ torsion angles are similar when captured from the first 5 ns of the trajectory (SMD1), the complete 30ns trajectory or a 90 ns-long duplicate simulation (SMD2). This control confirms that our SMD simulations are sufficiently long to provide a reliable approximation of the backbone flexibility.

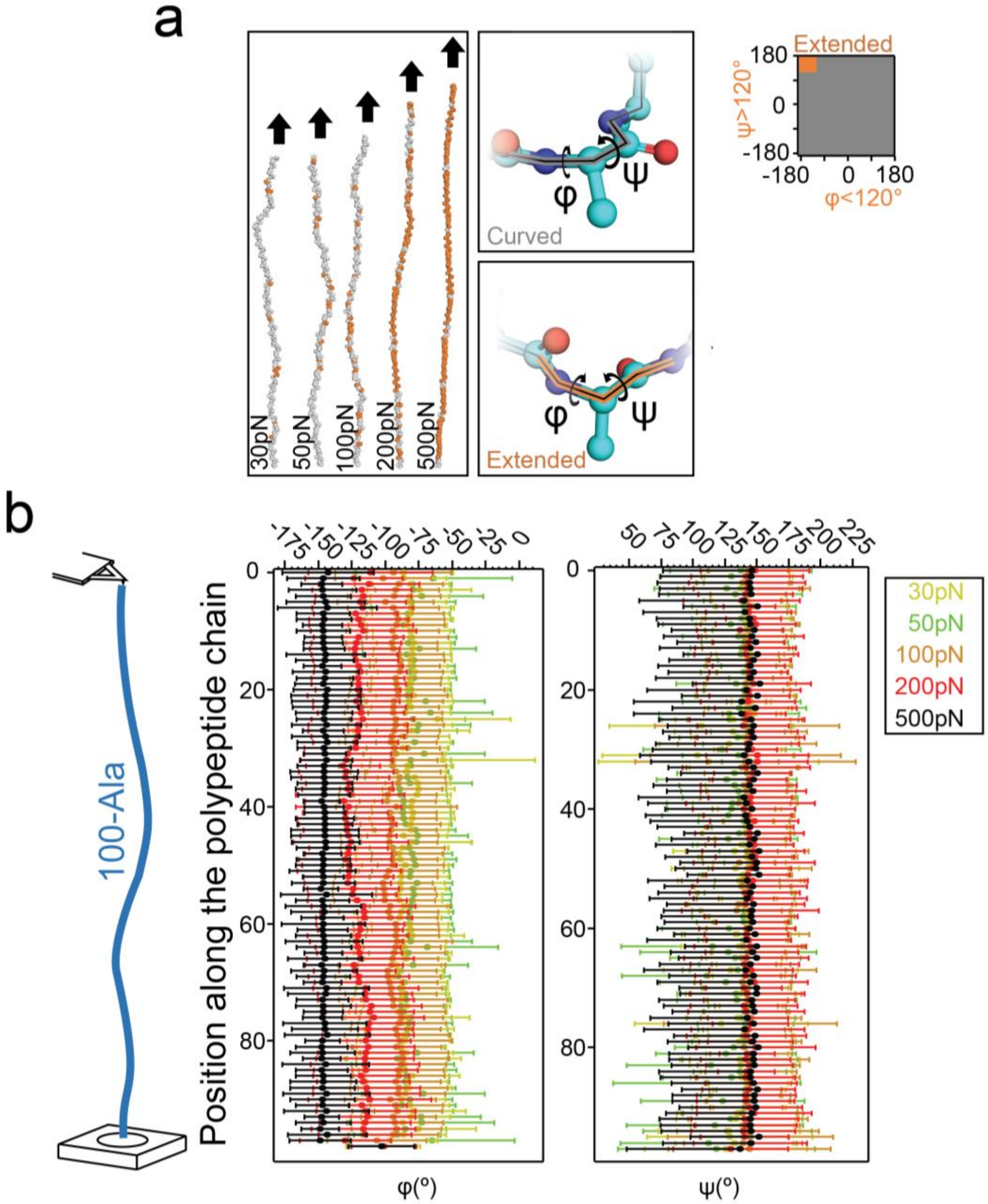

Fig. S8

Local curvature of the backbone decreases with force. ***a.*** For representative conformations along the SMD trajectories, we distinguish here the curved (orange, $-180° < \varphi < -120°$, $120° < \psi < 180°$) and extended states (grey) of the backbone. We observed that the occurrence of "curved" amino acid decreases when the force increases independently to the position along the chain. ***b.*** For each snapshot of SMD trajectories after reaching equilibrium, we measured the average and standard deviation of φ and ψ angles. Torsional angles of the backbone are homogenous and independent of the amino acid position in the polypeptide chain (100 alanine residues). The increase of force affects mostly φ and more moderately ψ. The fast internal friction of the stretched peptide is illustrated here by the local deformation in equilibrium along the chain.

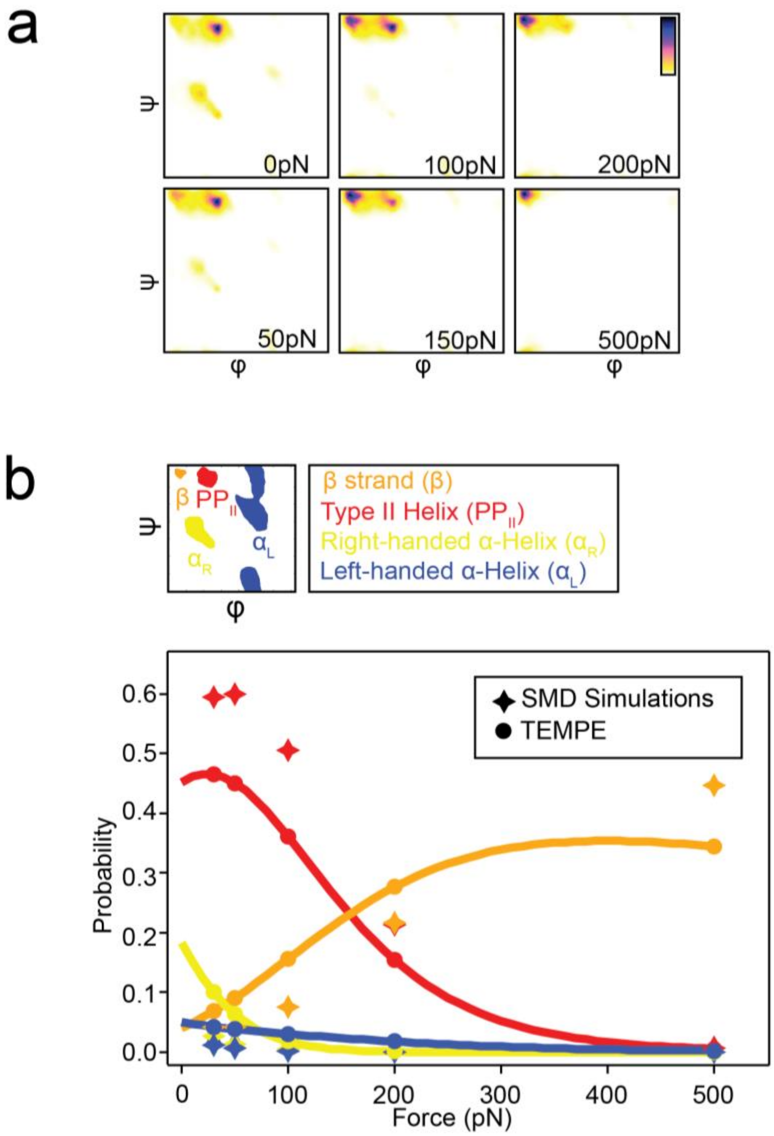

Fig. S9

Comparison of the SMD and the TEMPE approaches. ***a.*** Heatmaps representing the probability density calculated from the TEMPE method (Torsional Energy Model of Protein Elasticity). The heatmaps are similar to the ones obtained from SMD simulations (Fig. S7). In the color bar, white represents a zero-probability and blue the highest probability (2.10^{-3}). ***b.*** We defined four states, corresponding to the bottom of the free-energy basins and associated to distinct secondary structures (β strand, Type II Polyproline Helix, right-handed α-helix and left-handed α-helix). They are representative of the accessible space (sum of probabilities>0.5). We compare the probability to visit these states calculated from the SMD trajectories (stars) and from TEMPE in [0-500]pN range of force. The most populated basins, PP_{II} and β, show a two-regimes force dependency. At high force, the β state becomes dominant at the expense of the other three states (α_L, α_R and PP_{II}). The SMD simulations probably overestimate the prominence of deep basins at the expense of the large ensemble of high-energy states that are rarely accessible for the simulation time-scale.

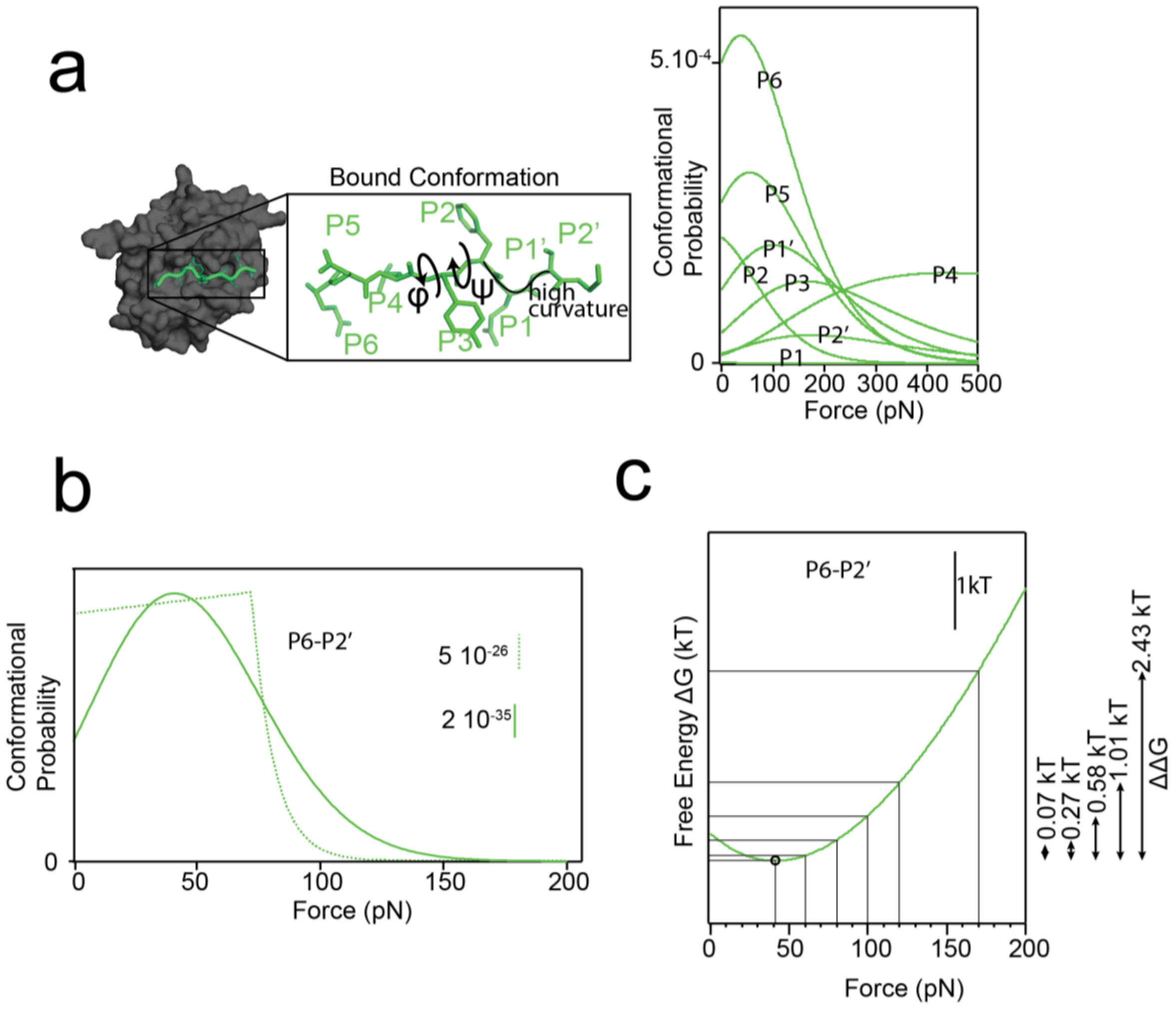

Fig S10

Role of conformational entropy upon the binding. a. Curvature of the backbone P6-P2' substrate (in green) in the holo structure of the Tev enzyme (left panel) (3). The right panel displays the probability to visit the bound conformation for each residue in P6-P2' deduced from the torsional free energy maps (TEMPE). The local curvature P6-P2' marked by dissimilar (φ ψ) values induces different force dependent probabilities. For instance, the residue P1 rarely visits its curved bound geometry. On contrary, P6 is frequently visited at ~0-100pN. This figure is reproduced in Fig. 7C with probabilities normalized to the maximum probability. **b.** Probability for P6-P2' to attain the bound conformation considering all possible accessible states (plain line) or only the state of minimal energy (dotted line). In this second approach, the probability was calculated from the difference of free energy between the state of minimum energy and the final bound state. Indeed, when all possible states are considered, we observe a better agreement to our experimental kinetics. For instance, we could observe enzymatic cleavage at 100pN. Furthermore, we validated this approach for a different system (14). **c.** Here , we report the impact of force as the difference in free energy ΔΔG (black circle) observed at the optimal force (41 pN) and the experimental forces 60 (0.07 kT, 1.44 kcal.mol^{-1}), 80, 100, 120 and 170pN (2.43 kT, 1.44 kcal.mol^{-1}).

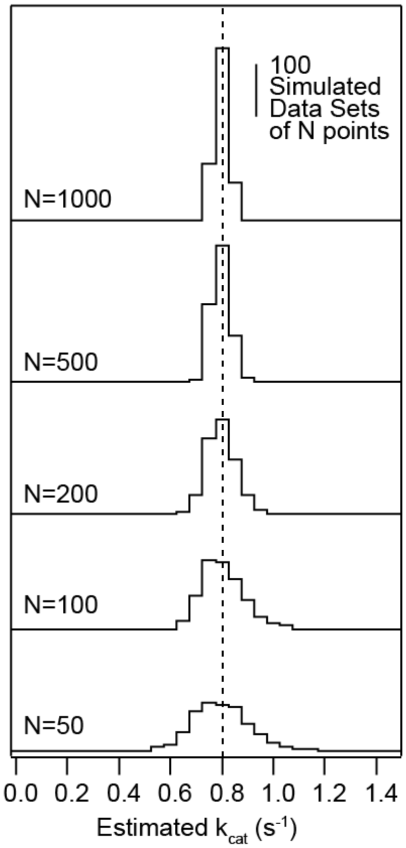

Fig S11

Estimation of the kinetic parameters from simulated dwell-time distributions. We show here the catalytic constants k_{cat} retrieved by fitting a 3-state model to 500 simulated distributions. Each of the 500 datasets contains N dwell time values stochastically generated with the experimental parameters k_{on} and k_{cat} (60pN, [Tev]=9μM). These simulations confirm the ability of the fit to retrieve k_{cat} (dotted line, 0.80 s^{-1}), especially for larger datasets. Crucially, our experimental dataset in Figure 4A contains N=456 measurements and appears large enough to build a reliable distribution.

2. Supplementary Tables

Force	**60 pN**		**80 pN**		**100 pN**	
	$\mathbf{k_{on}}$ **($M^{-1}.s^{-1}$)**	$\mathbf{k_{cat}}$ **(s^{-1})**	$\mathbf{k_{on}}$ **($M^{-1}.s^{-1}$)**	$\mathbf{k_{cat}}$ **(s^{-1})**	$\mathbf{k_{on}}$ **($M^{-1}.s^{-1}$)**	$\mathbf{k_{cat}}$ **(s^{-1})**
Constants	1.75e+5 ± 2.29e+4	0.80 ± 0.04	4.48e+4 ± 7.28e+3	0.75 ± 0.14	1.84e+4 ± 5.05e+3	0.57 ± 0.23
	1.78e+5 ± 1.79e+4	0.80*	4.31e+4 ± 4.09e+3	0.80*	1.57e+4 ± 2.26e+3	0.80*

*k_{cat} fixed to 0.80 s^{-1}

Table S1

Reactions rates retrieved from the dependence on the enzyme concentration and on the force applied to the substrate This table reports the constants *kon* and *kcat* deduced from fitting the models described by the equations eq.3 to the data (i.e. *krupture* for various conditions of [enzyme] and force applied to the substrate). We observed that *kcat* is moderately affected by the force in comparison to the striking force-dependency of *kon* revealed in the [60pN-100pN] force range.

Schechter and Berger	**Amino Acid**	**φ (º)**	**ψ (º)**
P6	E	-68.9	152.0
P5	N	-77.1	154.8
P4	L	-135.4	176.1
P3	Y	-142.8	140.0
P2	F	-68.8	131.7
P1	Q	-87.8	46.2
P1'	S	-84.7	165.2
P2'	G	-99.2	174.1

Table S2

Dihedrals of the substrate backbone in the bound conformation. Backbone dihedral angles of the bound conformation of the P6-P2’ substrate (Schechter and Berger nomenclature (15)), corresponding to the amino acid sequence ENLYFQSG, measured in the holo structure of the Tev protease (pdb: *1LVB*). We determined the limits of the substrate P6 and P2’ based on the presence of backbone-backbone hydrogen between the two partners in this region (Fig. S6c). We could not detect intermolecular hydrogen bonds beyond the peptide P6-P2’. It is worth mentioning here that the contribution of P2’ in the association, is probably modest, and to our knowledge, has not been evaluated in previous studies.

Residues	P6												X	X			X	X	X	X	
	P5							X					X	X				X	X	X	
	P4						X					X	X	X					X	X	X
	P3					X					X	X	X	X						X	X
	P2				X					X	X	X	X	X		X					X
	P1			X					X	X	X	X	X	X	X	X					
	P1'		X						X	X	X	X	X	X	X	X					
	P2'	X												X	X	X					
Slope		6.71E-05	3.79E-04	6.90E-07	2.99E-04	2.03E-04	7.81E-05	6.52E-04	1.21E-10	1.89E-14	1.67E-18	5.35E-23	8.91E-30	2.67E-34	3.56E-15	5.48E-19	1.09E-03	3.40E-07	1.23E-11	1.22E-15	1.02E-12
Pearson Coefficient	$k_{rup.}$	-0.97	-0.86	0.90	0.97	-0.97	-0.97	0.89	0.92	0.89	0.92	0.97	0.97	0.99	0.95	0.93	0.95	0.94	-0.85	-0.95	-0.88
	k_{on}	-0.94	-0.91	0.92	0.93	-0.94	-0.91	0.76	0.93	0.91	0.91	0.93	0.95	0.96	0.94	0.94	0.94	0.86	0.84	-0.91	-0.95

Table S3

Conformational entropy for the modeling of the force dependent reaction rates. This section reports the calculation of probabilities associated to the backbone configurations based on equilibrium statistical mechanics. Indeed, from the Ramachandran free-energy maps computed for different forces, we can estimate with the equation (ΔG = -kT.log(p)) the probability for one residue to visit the bound conformation, which is directly related to the free-energy cost to bring a given dihedral angle to its specific value in the bound complex. To distinguish the likelihood of this model, we compare the measured kinetics and the theoretical modeling (Fig. 7D).

The free energy model predicts the probability *pi* to visit the backbone conformation of each residue *i* (±1°) in the P6-P2' peptide (columns 1 to 7 and 16). The Pearson correlation coefficient aims to testing the strength of relationship at different forces (40pN, 60pN, 80pN, 100pN, 120pN) between this dimensionless probability and the measured rates $k_{rupture}$ and k_{on} (two last lines).

The slope of the simple linear regression line (obtained for the fit to $k_{rupture}$) indicates the different scales of the relative probabilities. Similarly, the probability *p* for *N* consecutive residue conformations in P6-P2' (considered residues marked with a X) is the product of probability *p* ($p = \prod_{i=2}^{N} pi$). A strong correlation is observed for positive Pearson coefficients close to the ideal value 1. The model fits better considering the conformation of a peptide rather than single residues (columns 1, 2, 4, 5, 6, 7 and 13). The strongest correlation (in red) is obtained for the complete substrate P6-P2' (Fig. 7D).

4. Supplementary Movie

The movie S1 presents the maps calculated with the TEMPE approach in a range of force from 0 to 500pN. Each frame displays the free energy map at a given force. The color code is similar (0-11kT) to the one presented in the figure 6B.

5. Supplementary References

1. Giganti D, et al. (2013) Conformational plasticity of the essential membrane-associated mannosyltransferase PimA from mycobacteria. *J Biol Chem* 288(41):29797–29808.
2. van den Berg S, Löfdahl P-A, Härd T, Berglund H (2006) Improved solubility of TEV protease by directed evolution. *J Biotechnol* 121(3):291–8.
3. Phan J, et al. (2002) Structural basis for the substrate specificity of tobacco etch virus protease. *J Biol Chem* 277(52):50564–50572.
4. Nunn CM, et al. (2005) Crystal structure of tobacco etch virus protease shows the protein C terminus bound within the active site. *J Mol Biol* 350(1):145–155.
5. Lu HP, et al. (1998) Single-molecule enzymatic dynamics. *Science* 282(5395):1877–82.
6. Kou SC, Cherayil BJ, Min W, English BP, Xie XS (2005) Single-molecule Michaelis-Menten equations. *J Phys Chem B* 109(41):19068–19081.
7. Broek B Van Den, Noom MC, Wuite GJL (2005) DNA-tension dependence of restriction enzyme activity reveals mechanochemical properties of the reaction pathway. 33(8):2676–2684.
8. Phillips JC, et al. (2005) Scalable molecular dynamics with NAMD. *J Comput Chem* 26(16):1781–1802.
9. Tropea JE, Cherry S, Bagossi P, Copeland TD (2005) Comparison of the substrate specificity of two potyvirus proteases. 272:514–523.
10. Giganti D, et al. (2015) Secondary structure reshuffling modulates glycosyltransferase function at the membrane. *Nat Chem Biol* 11(1):16–8.
11. Arnold U, Köditz J, Markert Y, Ulbrich-Hofmann R (2009) Local fluctuations vs. global unfolding of proteins investigated by limited proteolysis. *Biocatal Biotransformation* 23(3–4):159–167.
12. Garcia-Manyes S, Brujić J, Badilla CL, Fernández JM (2007) Force-clamp spectroscopy of single-protein monomers reveals the individual unfolding and folding pathways of I27 and ubiquitin. *Biophys J* 93(7):2436–2446.
13. Bustamante C, Marko J, Siggia E, Smith S (1994) Entropic elasticity of lambda-phage DNA. *Science (80-)* 265(5178):1599–1600.
14. Perales-Calvo J, Giganti D, Stirnemann G, Garcia-Manyes S (2018) The force-dependent mechanism of DnaK-mediated mechanical folding. *Sci Adv* 4(2). doi:10.1126/sciadv.aaq0243.
15. Schechter I, Berger a (1968) On the active site of proteases. 3. Mapping the active site of papain; specific peptide inhibitors of papain. *Biochem Biophys Res Commun* 32(5):898–902.